Li et al. *Zool. Res.* 2026, 47(1): 17−31
https://doi.org/10.24272/j.issn.2095-8137.2025.258
https://cstr.cn/32248.14.zr.2025.258

ZR | Zoological Research

Article Open Access

Host immune constraints delineate the window of microbial colonization during early development of *Larimichthys crocea*

Ruo-Jing Li[1], Zhen-Jun Zhuang[1], Zhao-Qiu Qu[1], Xin Yi[1], Qian-Wen Min[1], Biao Yuan[1], Jia-Yu Zhou[1], Xu-Bing Ba[1], Na Zhao[1,*], Bo Zhang[1,*]

[1] *Southern Marine Science and Engineering Guangdong Laboratory-Zhanjiang*, *Zhanjiang*, *Guangdong* 524025, *China*

ABSTRACT

Microbiota assembly during early ontogeny in teleost fish plays a central role in shaping immune maturation and establishing host-microbe homeostasis, yet the regulatory mechanisms driving microbial succession across key developmental windows remain poorly understood. In this study, *Larimichthys crocea* was used to delineate microbiota assembly dynamics and the impact of stochastic and deterministic processes. Results indicated that community assembly peaked at day 18 post-hatching (DPH18), coinciding with the highest neutral model fit (R^2=0.71) and migration rate (m=0.88). Alpha (α)-diversity exhibited a hump-shaped pattern, with *Comamonas* dominance inversely correlating with *Vibrio* at DPH18. Microbial source tracking indicated that host-associated taxa played a more prominent role than dietary or environmental sources. Transcriptomic profiling revealed pronounced immune modulation during early development. Pro-inflammatory signaling, including IL-17 pathway activation, was elevated prior to DPH18, while anti-inflammatory regulators, such as transforming growth factor beta 2 (*tgfb2*), declined over time, consistent with a transient reduction in immune restraint. Immune constraints in dexamethasone-treated zebrafish produced intestinal barrier impairment and microbial dysbiosis, demonstrating functional consequences of compromised early immune regulation. Collectively, these patterns defined DPH3–DPH18 as a critical colonization window in *L. crocea*, during which reduced immune constraint facilitates niche establishment by early colonizers. This temporally restricted window optimizes microbial resilience and long-term resistance to dysbiosis, providing a mechanistic basis for early-life microbiota-directed strategies in teleost development.

Keywords: Teleost microbiota; Microbial community assembly; Early development; Immune constraints

INTRODUCTION

The establishment and succession of early-life microbiota in teleost fish serve as pivotal determinants of growth trajectories, immune development, and long-term physiological outcomes (Deng et al., 2025; Nunez et al., 2025). Emerging evidence has implicated host biology, microbial dynamics, and environmental variables as key regulators of microbial community assembly during ontogeny (Hou et al., 2024b; Rimoldi et al., 2025; Woelfel et al., 2024). Host-driven selection, mediated by genetic architecture, physiological state, and immune maturation, critically shapes the incorporation or exclusion of pioneer taxa during early colonization (Bandara et al., 2024; Peng et al., 2024; Zhao et al., 2022). This selective filtering is further modulated by host developmental stage, introducing temporal variability that complicates efforts to elucidate the mechanisms underlying microbial assembly (Paralika et al., 2023). Environmental factors, such as diet and rearing conditions, can interact with host filtering either synergistically or antagonistically, further shaping the microbial community (Fernandes et al., 2022; Hou et al., 2024a; Marangon et al., 2023). Although existing studies consistently demonstrate that both biotic and abiotic factors modulate microbial assembly, the relative dominance of stochastic colonization versus deterministic host selection during early-life stages remains controversial (Burns et al., 2016; Lu et al., 2022; Zhao et al., 2024).

Exposure to aquatic pathogens during embryonic and larval development increases susceptibility to bacterial infections, compromises health, and elevates mortality risk in early-stage fish (Arevalo et al., 2023; Ba et al., 2025; Rosado et al., 2022). This heightened vulnerability reflects the ongoing reorganization of the immune system during early post-hatching stages, prior to the onset of immune competence (Schuh et al., 2020). Maternally derived immune components,

Received: 21 July 2025; Accepted: 26 August 2025; Online: 27 August 2025

Foundation items: This work was supported by the Southern Marine Science and Engineering Guangdong Laboratory (Zhanjiang) (ZJW-2023-01), Guangdong Basic and Applied Basic Research Foundation (2023A1515010576, 2024A1515012859), and Marine Youth Talent Project of Zhanjiang (2023E0006)

*Corresponding authors, E-mail: penguinzn@163.com; zb611273@163.com

such as IgM, lysozymes, and complement proteins, confer transient protection during embryogenesis (Pan et al., 2025), but their functional activity declines rapidly post-hatching. Consequently, larval defense relies predominantly on innate immunity until key adaptive organs—including the thymus and kidney—fully mature (Auclert et al., 2024; Sun et al., 2025). This developmental lag creates a temporal window of immune permissiveness, analogous to the "window of opportunity" described in mammals such as humans and mice (Gensollen et al., 2016; Ignacio et al., 2024; Nie et al., 2025), during which microbial exposure educates the naïve immune system in a temporally restricted manner. In humans, transcriptomic and functional analyses of early-life immune cells, such as regulatory T cells (Tregs), have revealed a phenotype adapted to a suppressive immune environment (Darrigues et al., 2018; Yin et al., 2021). A comparable window has been identified in turbot (*Scophthalmus maximus*), with the first 10 days post-hatching representing a critical window for microbial colonization (Gomes et al., 2025). Furthermore, in European eel (*Anguilla anguilla*), incomplete immune development during early stages impairs microbial regulation, suggesting a trade-off that suppresses pro-inflammatory responses to promote tissue tolerance and niche establishment (Bandara et al., 2024). These findings collectively support the hypothesis that teleost larvae may adopt an evolutionarily conserved strategy of transient suppression of pro-inflammatory responses to facilitate microbial colonization during this window. Although this strategy may increase infection susceptibility in the short term, it is likely to enhance long-term immune education and microbial homeostasis.

The present study investigated microbiota assembly dynamics in *Larimichthys crocea*, a marine teleost, to identify dominant ecological and host-associated forces shaping microbial community succession during early ontogeny. Using an integrated approach combining 16S rRNA gene sequencing, host transcriptomic profiling, and immune perturbation experiments in a zebrafish model, this study characterized the temporal interplay between immune activity and microbiota colonization. Therefore, we propose that *L. crocea* larvae undergo a developmental phase of reduced immune activation to facilitate microbial niche establishment. This transient immune permissiveness appears essential for stabilizing host–microbiota interactions and optimizing long-term resistance to dysbiosis, providing a mechanistic foundation for early-life microbial interventions in teleost health management.

MATERIAL AND METHODS

Ethics statement

All animal procedures were conducted in accordance with guidelines approved by the Animal Welfare Committee of the Southern Marine Science and Engineering Guangdong Laboratory-Zhanjiang, China (license number: 202407086).

Experimental design and sample collection

Larimichthys crocea larvae were obtained from Donghai Island farm in Zhanjiang, Guangdong, China. Fish were temporarily maintained in cylindrical tanks (radius: 2 m, depth: 1.2 m) under controlled conditions (24.5±1°C, pH: 7.8±0.3, dissolved oxygen: 6.6±2 mg/L, salinity: 28‰). Rearing water originated from a single impounding pond and underwent ultraviolet (UV) irradiation and biofiltration pretreatment. A 30% daily water renewal was maintained to ensure stable environmental inputs. Feeding followed a staged protocol reflecting ontogenetic nutritional requirements. Larvae were fed rotifers (R) from 4 to 9 days post-hatching (DPH), *Artemia* (A) from DPH10, water fleas (F) from DPH19–DPH29, and artificial feed (D) from DPH30 onwards (Figure 1), following standard

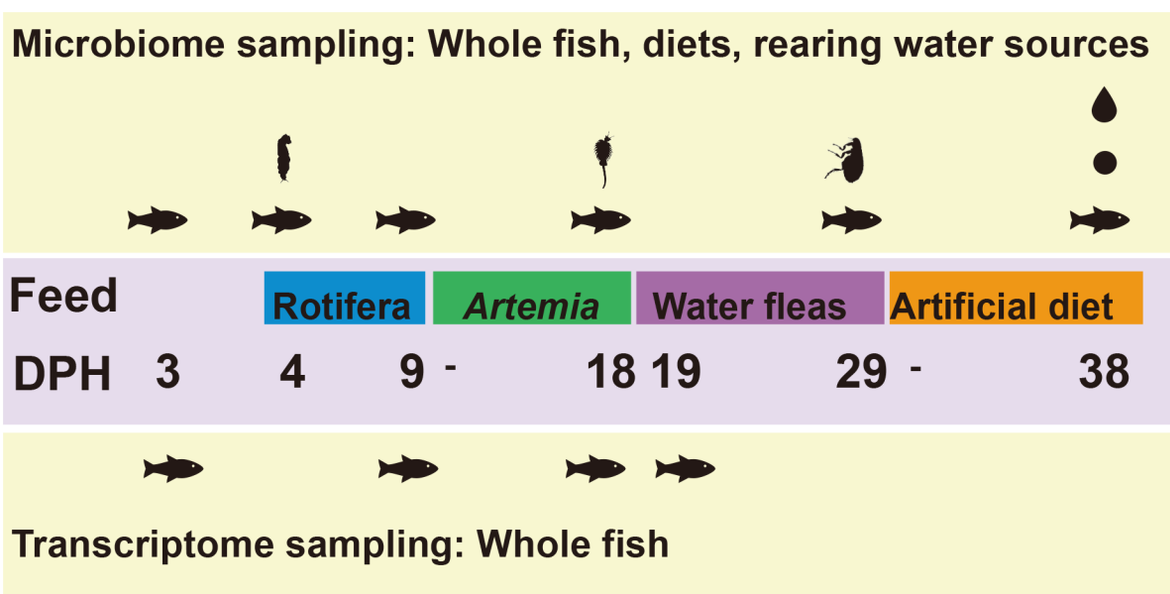

Figure 1 Sampling stages during early development of *Larimichthys crocea*

Fish were sampled across a 35-day period. Icons above and below the purple bar indicate corresponding time points and sample types used for microbiome and transcriptomic analysis. DPH, days post-hatching. DPH3, endogenous nutrition phase; DPH4, onset of swim bladder formation and transition to exogenous nutrition with rotifer feeding; DPH9, initiation of voluntary feeding; DPH18, final larval stage with *Artemia* feeding; DPH29, juvenile stage with water flea feeding; DPH38, fingerling stage with artificial diet (black dot). Water samples (black water drop) were sampled at DPH38. Silhouettes of rotifers, *Artemia*, and water fleas were obtained from PhyloPic (http://phylopic.org), available under a CC-BY 3.0 license (https://creativecommons.org/licenses/by/4.0).

marine fish larval-rearing procedures (Liu et al., 2024).

For microbiome and transcriptome analyses, larvae were randomly pooled, rinsed three times with sterile saline, anesthetized on ice, snap-frozen in liquid nitrogen, and stored at −80°C in Eppendorf (EP) tubes. Due to the small size of individual larvae, 5–8 individuals were pooled per biological replicate. For 16S rRNA gene sequencing, samples were collected from six developmental stages: DPH3 (endogenous nutrition), DPH4 (exogenous feeding initiation, rotifer feeding), DPH9 (voluntary feeding established), DPH18 (late larval stage, *Artemia* feeding), DPH29 (juvenile stage, water flea feeding), and DPH38 (fingerling stage, artificial diet), each with three biological replicates. Microbial inputs from feed types (R, A, F, and artificial diet) and the rearing water sources (DPH38) were also sampled in triplicate. Transcriptome sequencing focused on four timepoints spanning the early colonization window: DPH3 (baseline immunity prior to exogenous feeding), DPH9 (colonization under rotifer diet), DPH18 (peak microbial colonization), and DPH19 (transition to water flea feeding). These stages were selected to capture host immune transcriptional responses during early microbial establishment. Later stages (DPH29 and DPH38), when adaptive immune development progresses beyond the window of interest, were not included. Whole larvae were used for both microbiome and transcriptome analysis to ensure consistency (Gomes et al., 2025; Nikouli et al., 2019; Sumithra et al., 2024).

Zebrafish immune constraints model

A total of 90 healthy zebrafish (initial body weight: 0.21±0.03 g), procured from our own lab in Zhanjiang, were randomly assigned to one of three treatment groups, control (0 mg/L dexamethasone (DXMS), T1), low-dose (1 mg/L DXMS, T2), and high-dose (5 mg/L DXMS, T3). Fish were maintained in aquaria under standard conditions (25±1°C, pH 7.5–8.2, DO 5.7–8.3 mg/L) and fed *Artemia* twice daily for one week. Following anesthesia on ice, 12 individuals per group were dissected to obtain intestines, spleens, and dorsal skin samples. Tissues were divided into three aliquots for RNA and DNA extraction (stored at –80°C), histological analysis (intestines fixed in 4% paraformaldehyde), and biochemical assays (three whole fish, stored at –80°C). An additional three fish per group were stored whole at –80°C for biochemical analysis.

Microbiome analysis

Total DNA was extracted from homogenized *L. crocea* larvae collected at six developmental stages (DPH3, DPH4, DPH9, DPH18, DPH29, and DPH38) using an E.Z.N.A.® DNA Kit (Omega Bio-tek, USA) according to the manufacturer's protocols. DNA purity and concentration were assessed using 1% agarose gel electrophoresis and quantified using an ND-2000 UV-vis spectrophotometer (Thermo Scientific, USA). DNA was diluted to a final concentration of 1 ng/μL for amplification. The V3–V4 regions of the bacterial 16S rRNA gene were amplified using the universal primer pair 341F (5'-CCTACGGGNGGCWGCAG-3') and 806R (5'-GGACTACHVGGGTATCTAAT-3'). Amplified products were visualized on 2% agarose gels for confirmation, purified using AMPure XP beads (Beckman Coulter, USA), and re-amplified for indexing. Purified amplicons were quantified using a Qubit dsDNA High-Sensitivity Assay Kit (Thermo Fisher Scientific, USA) and pooled in equimolar concentrations. The final pooled library was subjected to paired-end sequencing on the Illumina PE250 platform. Raw sequencing reads were demultiplexed and quality-filtered using USEARCH (v.9.2.64) with default parameters. Operational taxonomic units (OTUs) were clustered at 97% sequence similarity using the UPARSE algorithm, and chimeric sequences were removed via reference-based detection against the RDP Classifier (v.1.6). Representative sequences for each OTU were annotated using the SILVA 138 reference database. Functional profiles were predicted using PICRUSt2 (v.2.1.4) based on Kyoto Encyclopedia of Genes and Genomes (KEGG) pathway annotations. Microbial phenotypes were inferred using BugBase.

SourceTracker analysis

The relative contributions of potential microbial sources to the larval gut microbiota across developmental stages were estimated using SourceTracker based on a Bayesian framework proposed by Knight et al. (2011). Pre-feeding stage larvae, larvae from each timepoint, and dietary components (rotifers, *Artemia*, water fleas, artificial diet) were designated as source communities, while larval gut communities from seven developmental stages (DPH3–DPH38) were treated as sinks. Analyses were performed in R (v.4.3.1) using the parameters: rarefaction depth=1 000, burn-in=100, restarts=10, and α=0.001.

Neutral community model and null model analyses

Sloan's Neutral Community Model (NCM) was implemented in R to assess the relative contributions of neutral processes versus deterministic selection in shaping microbial community assembly. The model estimates goodness-of-fit (R^2), which represents the proportion of community variation explained by neutral dynamics, and the immigration rate (m), which represents the probability of dispersal from a metacommunity source (Chen et al., 2019).

To further resolve the underlying ecological processes, null model analysis was performed based on phylogenetic turnover between communities. The β-nearest taxon index (βNTI) was calculated to infer the balance between deterministic and stochastic forces. Values of βNTI>2 indicate phylogenetic turnover greater than expected by chance, implying heterogeneous selection structuring community assembly. Values of βNTI<–2 suggest dominance of homogeneous selection. Values of |βNTI|≤2 suggest dominance of stochastic processes, such as drift. βNTI values were computed using the "picante" (v.1.8.2) R package and visualized with "ggplot2" (v.3.5.2).

Transcriptomic analysis

Whole-body RNA was extracted from *L. crocea* larvae at four developmental stages (DPH4, DPH9, DPH18, and DPH19; *n*=3 replicates per stage) using TRIzol Reagent (Vazyme, China). RNA integrity was verified by 1% agarose gel electrophoresis to confirm the absence of degradation or contamination. RNA purity (A260/A280>1.8), concentration, and integrity were quantified using a NanoDrop 2000 spectrophotometer (Thermo Fisher Scientific, USA) and Agilent 2100 Bioanalyzer (Agilent Technologies, USA). Library construction and Illumina sequencing were conducted using the Illumina NovaSeq 6000 platform (USA). Raw reads were filtered to remove adapters and low-quality sequences (Q-score<20) using fastp (v.0.18.0). High-quality reads were aligned to the *L. crocea* reference genome (GCF_000972845.2) using HISAT2 (v.2.10). Differentially expressed genes (DEGs, |log2FC|≥2, *P*<0.05) were identified

using DESeq2 (v.1.38.3). KEGG pathway enrichment was performed via the BioCloud platform (https://www.biocloud.net/).

Integration of microbiome and transcriptomic analyses

Covariation analysis was conducted to identify associations between microbial composition and host immune gene expression. All DEGs annotated to immune-related pathways were first compiled, and 11 immune-associated candidate genes with frequent occurrence and significance were selected. Genes significantly correlated with microbial taxa (P<0.05) were used to generate a signature set for KEGG enrichment, from which five pathways were selected based on a false discovery rate (FDR)<0.1. Pearson correlation coefficients were calculated to assess the relationship between immune-related gene expression and the relative abundance of six representative microbial genera (*Comamonas*, *Tenacibaculum*, *Nautella*, *Vibrio*, *Acinetobacter*, and *Bacillus*). Seven genes showing significant associations were selected for visualization. A correlation heatmap was generated using the OmicShare heatmap visualization tool (https://www.omicshare.com/tools).

Quantitative real-time polymerase chain reaction (qPCR)

Total RNA was extracted from zebrafish intestinal and splenic tissues using TRIzol Reagent (Invitrogen, USA) following the manufacturer's protocols. RNA integrity was confirmed by 1% agarose electrophoresis, and purity was confirmed by A260/A280>1.8. High-quality RNA was reverse transcribed using PrimeScript™ RT Master Mix (Takara, Japan), and resulting cDNA was stored at –80°C. Primers for immune-related genes (*tgfb2*, chemokine (C-C motif) ligand 25a (*ccl25a*), complement component 1, q subcomponent, B chain (*c1qb*), signal transducer and activator of transcription 1a (*stat1a*), matrix metallopeptidase 9 (*mmp9*), complement component 9 (*c9*), C-X-C motif chemokine ligand 8 (*cxcl8*)) and intestinal barrier genes (tight junction protein 1a (*tjp1a*), claudin b (*cldnb*), claudin 15-like a (*cldn15la*), catenin beta 1 (*ctnnb1*), mucin 5.1 (*muc 5.1*), and mucin 2.1 (*muc2.1*)) were designed using Primer Premier v.5.0 (Supplementary Table S1) and verified via BLASTn. Relative gene expression was normalized to *β*-actin and calculated using the $2^{-\Delta\Delta CT}$ method (Livak & Schmittgen, 2001).

Species-specific qPCR for bacterial quantification

Genomic DNA was extracted from zebrafish tissues using a commercial reagent kit (TIANGEN Biotech, China), following the manufacturer's procedures. Genus-specific primers targeting *Vibrio*, *Bacillus*, and *Acinetobacter* were designed based on previously published methods (Kim et al., 2019; Wei et al., 2023). qPCR was performed in 10 μL reactions containing 1 μL of DNA, 3.2 μL of ddH_2O, 5 μL of SYBR Green Master Mix (TransGen Biotech, China), and 0.4 μL of each primer using a LightCycler 96 system. Thermocycling conditions included an initial denaturation at 95°C for 30 s, followed by 40 cycles of 95°C for 10 s and 60°C for 15 s. Relative bacterial abundance was analyzed using the $2^{-\Delta\Delta CT}$ method with 338F/518R as a reference (Supplementary Table S1).

Histological staining

Fixed intestinal samples (n=3 per group) were dehydrated through a graded ethanol series, cleared with xylene, embedded in paraffin, and sectioned at 4 μm thickness. Sections were stained with Periodic Acid-Schiff (PAS) and hematoxylin and eosin (H&E). Stained tissues were imaged using an optical microscope (Olympus, Japan) and analyzed using SlideViewer (v.2.6.0). Each section was divided into four quadrants, and one villus was randomly sampled per quadrant. Morphometric parameters, including villus height and width, submucosa thickness, and lamina propria width, as well as other histopathological features, were quantified using ImageJ software (v.1.54f).

Determination of biochemical parameters

Whole-body zebrafish tissues were homogenized in ice-cold phosphate-buffered saline (PBS) and centrifuged (2 500 ×g, 10 min, 4°C) to obtain supernatants. Acid phosphatase (ACP) and alkaline phosphatase (AKP) activities were measured using commercial kits (Nanjing Jiancheng, China). Total protein (TP) was quantified using the BCA method (Nanjing Jiancheng, China), and enzymatic activities were normalized to protein content (U/gprot). Each treatment group included three biological replicates, with all assays performed in technical triplicates.

Bacterial isolation and identification

Homogenized *L. crocea* samples were serially diluted in sterile saline and plated on marine-specific 2216E agar for selective cultivation of halophilic microbiota. After static incubation at 28°C for 24 h–48 h, morphologically unique colonies were selected based on size, margin characteristics, and pigmentation, followed by three successive streak-plate purification cycles to obtain axenic cultures. For taxonomic classification, genomic DNA was amplified using universal primers 27F (5′-AGAGTTTGATCCTGGCTCAG-3′) and 1492R (5′-TACGACTTAACCCCAATCGC-3′) targeting the 16S rRNA gene. PCR was conducted in 25 μL reactions containing 12 μL of 2×Taq PCR Master Mix (Qiagen, Germany), 1 μL of each primer, 1 μL of DNA template, and 10 μL of ddH_2O. Amplification conditions were: 95°C for 5 min, 35 cycles at 94°C for 1 min, 55°C for 40 s, 72°C for 30 s, and a final extension at 72°C for 10 min. Purified amplicons were sequenced bidirectionally by Sangon Biotech (China). Consensus sequences were aligned against the NCBI nr/nt database using BLASTn, with species delineation thresholds set at ≥97% 16S rRNA similarity. Phylogenetic reconstruction was performed in MEGA-X (v.10.2.2) via the neighbor-joining method (Kumar et al., 2018), with evolutionary distances computed using the Kimura 2-parameter model (bootstrap=1 000 replicates).

Bacterial growth

Isolated strains were cultured in LB broth supplemented with 0 mg/L, 1 mg/L, and 5 mg/L DXMS, corresponding to treatment groups T1, T2, and T3, respectively. Growth was monitored by measuring the optical density at 600 nm (OD_{600}) in a 96-well microplate under microaerobic conditions. Cultures were incubated at 30°C in a Thermo Scientific™ Multiskan™ GO microplate reader (Thermo Fisher Scientific, USA), and OD_{600} readings were recorded hourly for 10 h starting from an initial inoculum of OD_{600}=0.1. Three independent biological replicates were performed for each experimental condition.

Statistical analysis

Linear and quadratic regression models were applied to genus-level abundance data and visualized using the "ggplot2" package in R (v.4.3.1). Alpha (α)-diversity indices (Shannon-Wiener index, Simpson, Chao1, and PD-whole-tree) were computed in QIIME2 (v.2020.11), and statistical

differences across developmental stages were assessed using the Kruskal-Wallis test. Beta-diversity analyses were conducted using principal component analysis (PCA), implemented with the "vegan" package (v.2.7.1) in R. Community composition differences were statistically validated using PERMANOVA (Adonis test, 999 permutations; P<0.05). Spearman correlation coefficients were used to assess relationships between diet and larval microbiota and visualized using the "corrplot" package (v.0.95) in R. All data are presented as mean±standard deviation (SD). Statistical analyses were performed using SPSS v.27.0 and R. Data normality (Shapiro-Wilk test) and homogeneity of variance (Levene's test) were first confirmed. For normally distributed data, one-way analysis of variance (ANOVA) followed by Bonferroni *post hoc* correction was applied. For non-normally distributed data, the Kruskal-Wallis test was applied. Statistical significance was defined as P<0.05.

RESULTS

Community structure, diversity and functional prediction of *L. crocea* larval and diet-associated microbiota

Microbial communities in *L. crocea* larvae, diets, and rearing water were taxonomically classified into 43 phyla, 100 classes, 275 orders, 393 families, and 772 genera. Across all sample types, Proteobacteria predominated, followed by Bacteroidetes, Firmicutes, and Planctomycetota (Figure 2A). No significant variation in the relative abundance of the top three phyla was observed from DPH3 to DPH38 (P>0.05). At the genus level, *Comamonas*, *Tenacibaculum*, *Nautella*, and

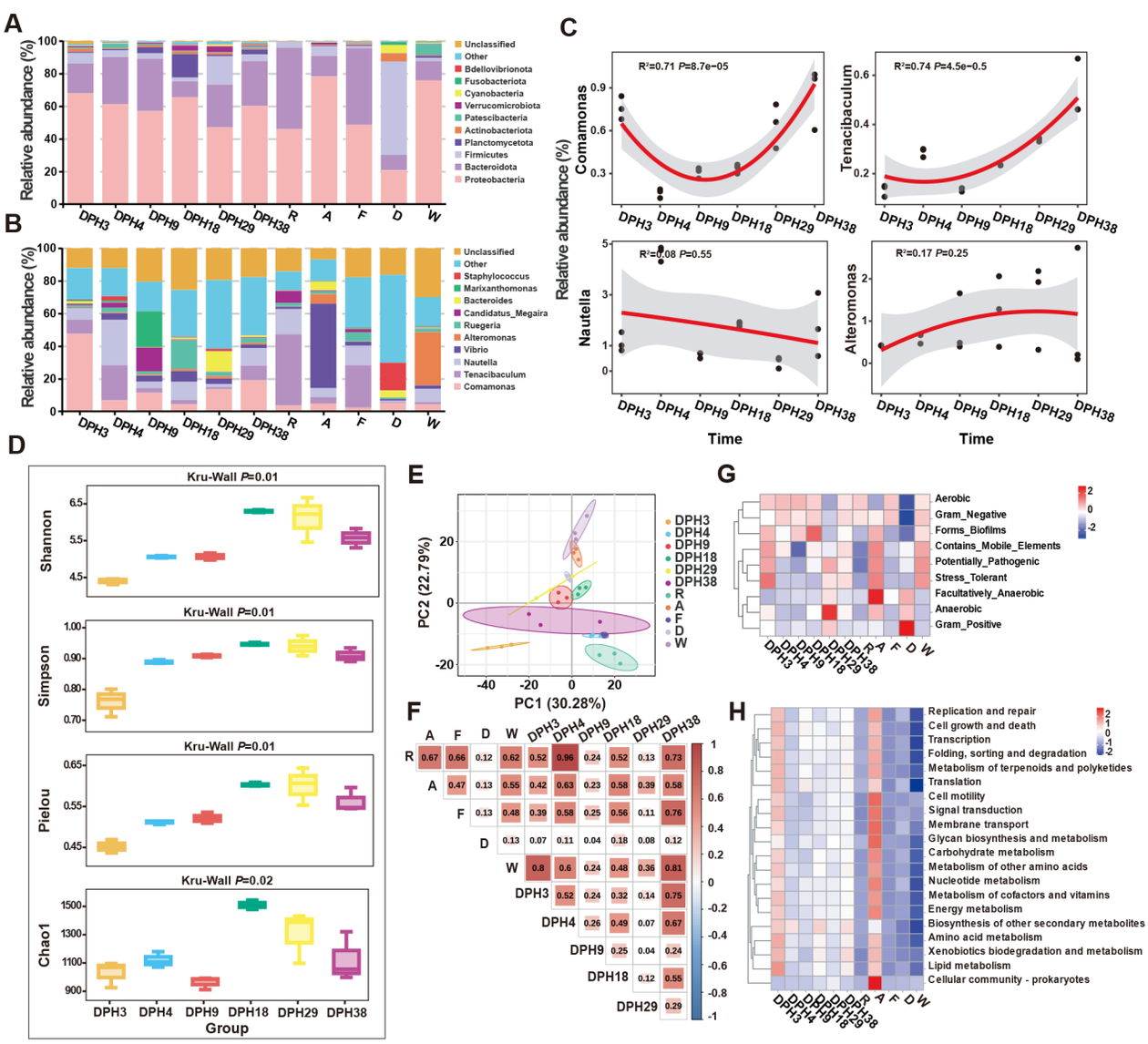

Figure 2 Community characteristics, and functions of *Larimichthys crocea* larval and dietary microbiota across early developmental stages

A: Microbial community composition of dietary sources and larval samples at the phylum level. B: Microbial community composition at the genus level. R: Rotifers; A: *Artemia*; F: Water fleas; D: Artificial diet; W: Rearing water. DPH: Days post-hatching. C: Relative abundance dynamics of dominant genera across developmental stages. D: Alpha diversity indices (Shannon, Simpson, Pielou, and Chao1) for larval microbiota. E: Principal component analysis (PCA) of dietary, water, and larval microbiota at the genus level. F: Spearman correlation analysis among diet, water, and larval microbial communities, with color intensity indicating correlation strength and red denoting positive correlation. G, H: Heatmaps showing predicted microbiota phenotypes and functional profiles generated using BugBase and PICRUSt2.

Vibrio were consistently detected in both larval and live-feed microbiota (Figure 2B). *Comamonas* exhibited a U-shaped pattern, with the lowest abundance at mid-developmental stages and a significant peak at DPH38 (P<0.05). *Tenacibaculum* increased progressively, reaching maximal abundance at DPH 38 (P<0.05). In contrast, *Nautella* declined gradually from DPH3 to DPH38, although without statistical significance (P>0.05). *Alteromonas* also showed an increasing trend but without significant differences (P > 0.05, Figure 2C).

Alpha diversity indices, including Shannon-Wiener, Simpson, Pielou, and Chao1, differed significantly across developmental stages (Kruskal-Wallis test, P<0.05), with diversity peaking at DPH18 before declining at later stages (Figure 2D). For community structure, PCA results revealed significant stage-specific clustering of larval samples. The first two principal components (PC1: 30.28%; PC2: 22.79%) collectively accounted for 53.07% of the total variance (Figure 2E). PERMANOVA (Adonis) confirmed significant dietary community divergence by stage (R^2=0.93, permutation test, P<0.001), with DPH3 showing clear separation from all diet samples.

Spearman correlation analysis revealed that microbial communities from R, A, F, and rearing water were positively associated with larval microbiota at DPH3, DPH4, DPH18, and DPH38 (r>0.5). Notably, DPH38 larvae exhibited the strongest correlations with R, A, F, and water microbiota (r>0.58), but showed only weak association with diet D (r=0.12). DPH29 larvae exhibited minimal correlation with all dietary and environmental sources (0<r<0.36), while diet D consistently showed weak correlations across all developmental stages (0<r<0.18) (Figure 2F).

BugBase-based phenotypic predictions identified nine functional microbial categories across stages. DPH3 and rearing water microbiota exhibited highly similar profiles, characterized by elevated abundances of Aerobic, Forms_Biofilms, Contains_Mobile_Elements, Potential_Pathogens, and Stress_Tolerant. Similarly, microbiota from DPH4 and DPH9 aligned with R-associated profiles, showing enrichment in Gram_Positive, Potential_Pathogens, Facultative_anaerobic, Anaerobic and Stress_Tolerant (Figure 2G).

PICRUSt2-based functional inference revealed distinct metabolic profiles among DPH3, diet A, and water communities. In contrast, predicted functional capacities at DPH4 and DPH9 were not strongly influenced by R-associated microbiota. Similarly, diets had limited functional impact on microbial communities at DPH18, DPH29, and DPH38 (Figure 2H).

Larval microbiota succession and microbial overlap with dietary sources

To investigate microbial transmission dynamics between diet and host, shared genera and OTUs were analyzed across larval developmental stages. A total of 149 bacterial genera were consistently shared between larvae and diets, with *Comamonas*, *Tenacibaculum*, *Nautella*, and *Vibrio* representing the most abundant taxa. Over 150 genera were shared among larval, diet, and rearing water samples, with diet D exhibiting the highest proportion of unique genera. Notably, water contributed more taxa to the larval microbiota than diets at several stages, particularly at DPH18 (Figure 3A). At the OTU level, seven, eight, four, and one OTU (average abundance >1%) were shared between larval and diet microbiota at successive stages. Among these, OTU_1 (*Comamona*s, Supplementary Table S2) persisted across the four developmental stages (Figure 3B–E). In addition, three, four, five, and four OTUs (average abundance >1%) were consistently shared between larvae and water across stages. OTU_1 (*Comamonas*), OTU_2 (*Nautella*), and OTU_5 (*Ruegeria*) remained consistently detected in larval and water communities across the full developmental series (Supplementary Figure S1A–D and Table S3).

Larval microbial source tracking and community assembly mechanisms

SourceTracker analysis identified pre-larval, larval, and stage-specific environmental reservoirs (diet and water) as the primary microbial sources contributing to larval gut communities. Endogenous larval sources accounted for the largest proportion of microbial input across all developmental stages (P<0.05), significantly exceeding contributions from diets and water. Moreover, environmental influences declined progressively as development proceeded (Figure 3F). Subsequently, NCM was used to quantify the influence of stochastic processes. Model fit peaked at DPH18 (R^2=0.71), followed by a decline to the lowest fit at DPH38 (R^2=0.60), suggesting a shift from stochastic to increasingly deterministic assembly over time (Figure 4B–D). Consistently, the estimated migration rate (m), reflecting microbial dispersal between communities, also peaked at DPH18 (m=0.88), indicating maximal microbial exchange at this stage. Additionally, neutrally distributed OTUs increased from 80.2% (DPH3) to 90.2% (DPH29), before decreasing sharply to 45.6% at DPH38, marking a transition toward deterministic selection post-DPH18 (Figure 4A–D).

To further resolve ecological processes, null model analysis based on βNTI values revealed clustering near –2 across stages, indicating a dominant role for homogeneous selection and dispersal limitation, with no significant variation across timepoints (Kruskal-Wallis P>0.05; Figure 4E). Overall, community assembly appeared to be governed primarily by homogeneous selection and limited dispersal, followed by a lesser contribution from heterogeneous selection (Figure 4F).

Differential gene expression highlights active immune modulation

Comparative transcriptomic profiling of *L. crocea* larvae across three developmental transitions (DPH3 vs. DPH9, DPH9 vs. DPH18, and DPH18 vs. DPH19) revealed extensive stage-specific immune modulation. A total of 3 229 DEGs (505 up-regulated and 2 724 down-regulated), 2 931 DEGs (1 903 up-regulated and 1 028 down-regulated), and 276 DEGs (144 up-regulated and 132 down-regulated) were identified across the respective comparisons (Figure 5A). PCA confirmed strong stage-specific transcriptional divergence, with PC1 (72.7%) and PC2 (17%) explaining 89.7% of the total variance (Figure 5B). Functional enrichment revealed that DEGs were significantly overrepresented in immune-related pathways, including complement and coagulation cascades and IL-17 signaling (Figure 5C). Compared to DPH3, DPH9 exhibited up-regulation of genes involved in leishmaniasis, pertussis, complement and coagulation cascades, and IL-17 signaling, indicative of innate immune activation. These pathways remained highly activated at DPH18. However, a striking reversal occurred at DPH19, with marked down-regulation of these same pathways, consistent with the onset of immune tolerance during later development (Figure 5D–F).

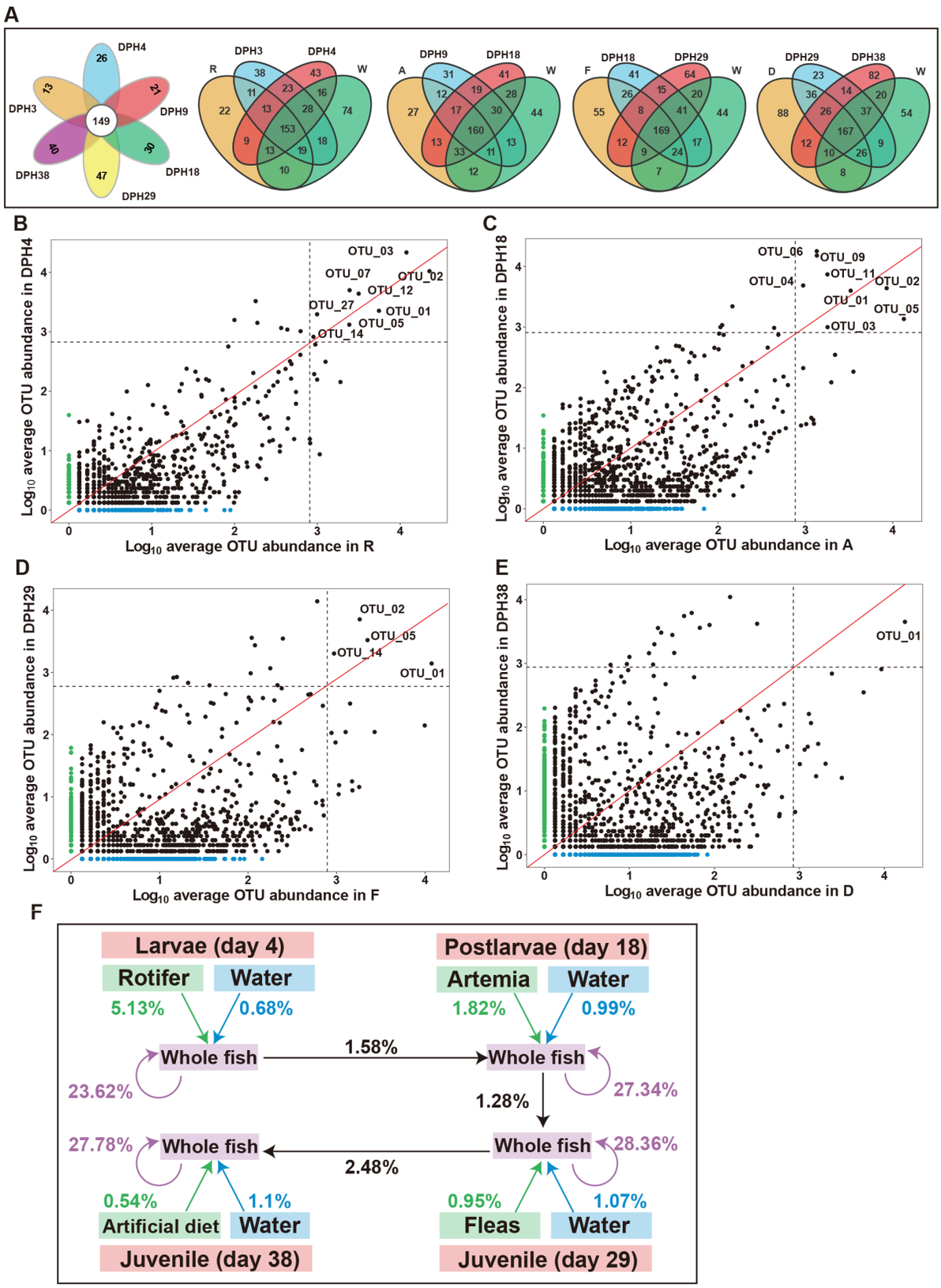

Figure 3 Succession of larval microbiota and biotic source contributions across development

A: Venn diagram showing shared genera between larval microbiota and biotic sources—rotifers (R), *Artemia* (A), water fleas (F), artificial diet (D), and water (W)—across developmental stages (DPH: Days post-hatching). B–E: Scatterplots of $\log_{10}$-transformed mean OTU abundance in larvae versus diet at DPH4, DPH18, DPH19, and DPH38. Dashed lines denote 1% abundance threshold. Labeled OTUs represent those enriched in both larvae and diet (mean abundance ≥1%), while unlabeled OTUs fall below the 1% threshold. Red diagonal: equal abundance in paired samples. F: Flowchart of SourceTracker analysis. Green lines represent contributions from corresponding diets; blue lines indicate water-derived sources; black lines denote carryover from prior larval stages; purple lines represent endogenous bacterial taxa present at the current stage. Mean contribution values are shown.

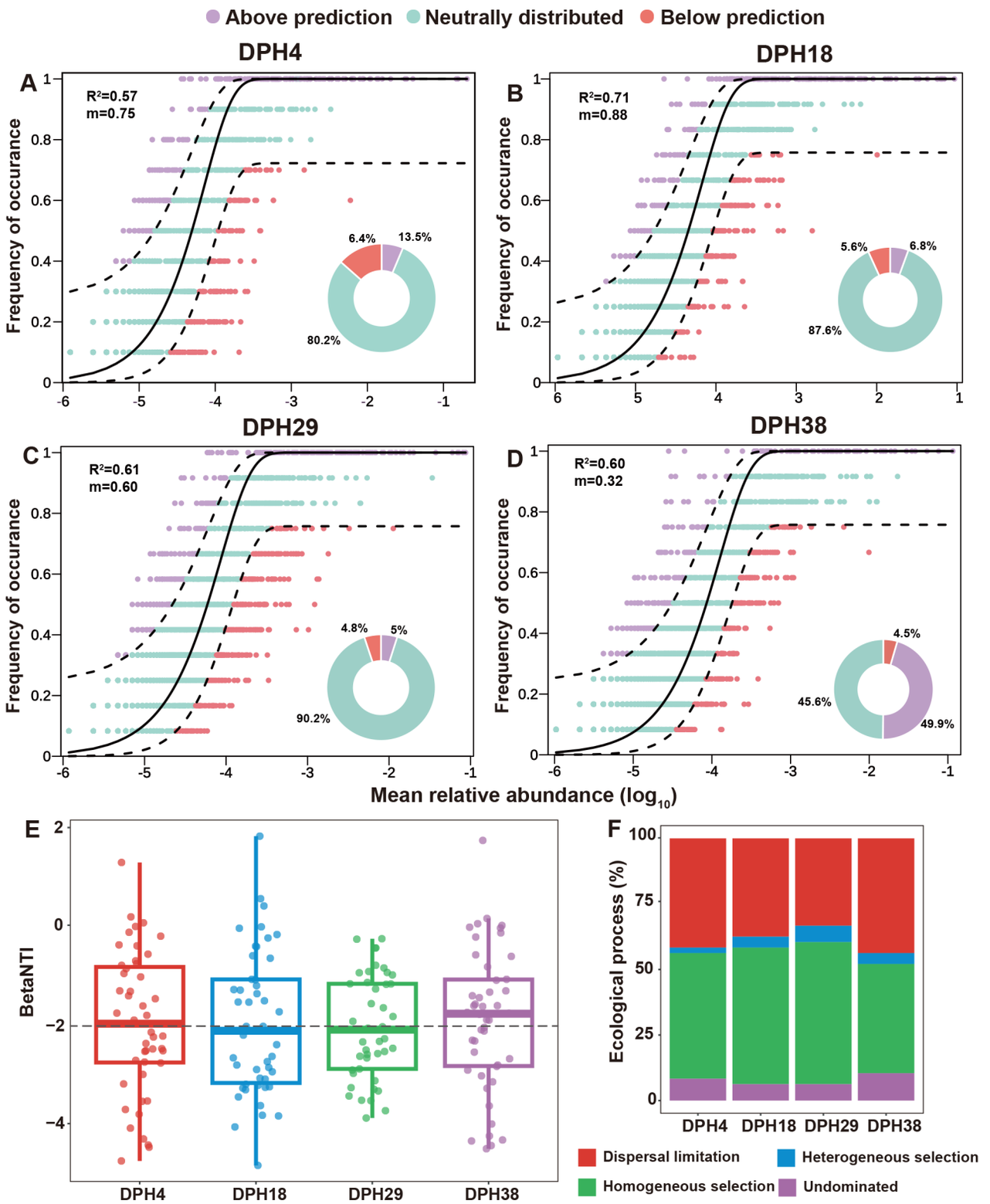

Figure 4 Neutral and null model fits for larval bacterial community assembly

A–D: Neutral model predictions for larval microbiota at four developmental stages. OTUs are color-coded: Purple (observed frequency>predicted), red (observed frequency<predicted), green (within 95% confidence intervals). Black line: Best-fit model; Dashed lines: 95% confidence intervals; R^2: Goodness-of-fit of neutral model; m: Estimated migration rate. E: Variation in βNTI values across developmental stages. βNTI>+2: Heterogeneous selection, βNTI<−2: Homogeneous selection, |βNTI|≤2: Stochastic processes. F: Relative contributions of ecological processes to community assembly.

Immune-related gene expression correlates with commensal abundance

To assess microbiota-immune crosstalk, 11 immune related genes—filtered from DEGs and enriched across eight immune pathways—were evaluated, including IFI30 lysosomal thiol reductase (*ifi30*), complement component 7b (*c7b*), complement component 3 (*c3*), CCAAT enhancer binding protein beta (*cebpb*), *c9*, *cxcl8*, *mmp9*, *tgfb2*, *stat1a*, *c1qb*,

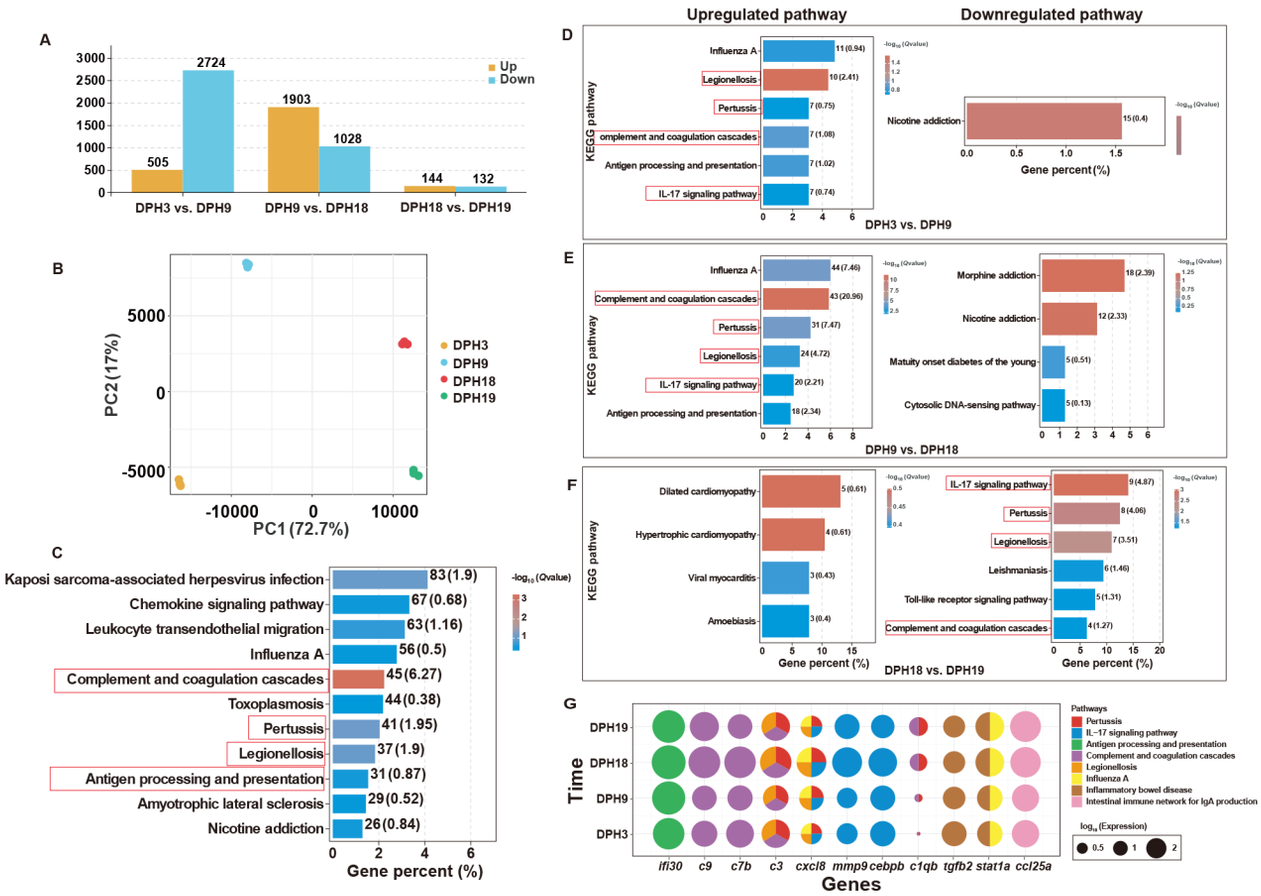

Figure 5 Differentially expressed immune-related genes across larval stages in *Larimichthys crocea*

A: Number of differentially expressed genes (DEGs) identified across larval stages. B: Principal component analysis (PCA) of transcriptomic profiles. C: KEGG pathway enrichment analysis of all DEGs. D–F: Immune-related KEGG pathway enrichment for pairwise comparisons: DPH3 vs. DPH9, DPH9 vs. DPH18, and DPH18 vs. DPH19. Left bar plots: Up-regulated pathways, right bar plots: Down-regulated pathways. Red squares: Pathways consistently enriched across all comparison groups. G: Heatmap of immune-related gene expression. Circle size: Log-transformed expression levels.

and *ccl25a*. Expression of *c9* and *c7b* peaked at DPH18, in line with the up-regulation of the complement and coagulation cascade. Similarly, *mmp9* and *cebpb* reached maximum expression at DPH18, aligning with activation of the IL-17 signaling pathway. Both *c3* and *cxcl8* also showed maximal expression at DPH18, with involvement in multiple immune pathways. In contrast, *tgfb2* expression was lowest at DPH18. While *stat1a* and *ccl25a* expression did not differ significantly between DPH18 and DPH19, both genes showed significantly higher expression at these later stages relative to DPH3 and DPH9. For *ifi30*, expression remained stable across developmental stages (Figure 5G).

Integrated analysis revealed significant enrichment of transcript-taxa associations within five immune-related KEGG pathways, including leishmaniasis, pertussis, antigen processing and presentation, epithelial cell signaling in *Helicobacter pylori* infection, and IL-17 signaling (Figure 6A). Network analysis revealed strong correlations between immune genes and dominant microbial taxa. Notably, heat shock protein (*hsp90aa1.a* and *hspa2*), complement C4B (*c4b*), ATPase H^+ transporting V1 subunit E1b (*atp6v1e1b*), and *cxcl8* exhibited strong associations with key microbial genera. *cxcl8* showed a significant positive correlation with *Acinetobacter* (Figure 6B). Interestingly, *tgfb2* exhibited a strong negative correlation with *Acinetobacter*, whereas the other eight genes showed positive associations, particularly *c9*, *mmp9*, *cxcl8*, *c7b*, and *c3* (Figure 6C). *Vibrio* displayed comparable correlation patterns as *Acinetobacter* but was positively associated with *ccl25a*, *c1qb*, and *stat1a*.

DXMS-induced immune constraints alter the commensal composition in zebrafish

DXMS treatment for 7 days significantly impaired immune function in zebrafish, as evidenced by dose-dependent reductions in ACP and AKP activities (P<0.05; Figure 7A), consistent with down-regulation of the corresponding genes in *L. crocea* transcriptomes (Figure 7B). Expression of *tgfb2*, *stat1a*, *c1qb*, *ccl25a*, and *mmp9* in the spleen decreased with increasing DXMS concentration (P<0.05). The expression levels of *cxcl8* and *c9* were lowest in the T2 group (P<0.05), while *tgfb2* and *c1qb* expression did not differ between the control (T1) and T2 groups (P>0.05) (Figure 7C). In parallel, DXMS exposure induced compositional shifts in core commensals. The relative abundance of intestinal *Acinetobacter* decreased with increasing DXMS concentrations, while skin-associated *Acinetobacter* was highest in the T3 group (P<0.05). *Bacillus* abundance declined significantly in the intestine, while skin abundance first increased and then decreased. *Vibrio* abundance declined in the skin but peaked in T2 in the intestine (Figure 7D, E). Temporal shifts in the abundance of *Acinetobacter* and *Vibrio* observed during *L. crocea* development were partially

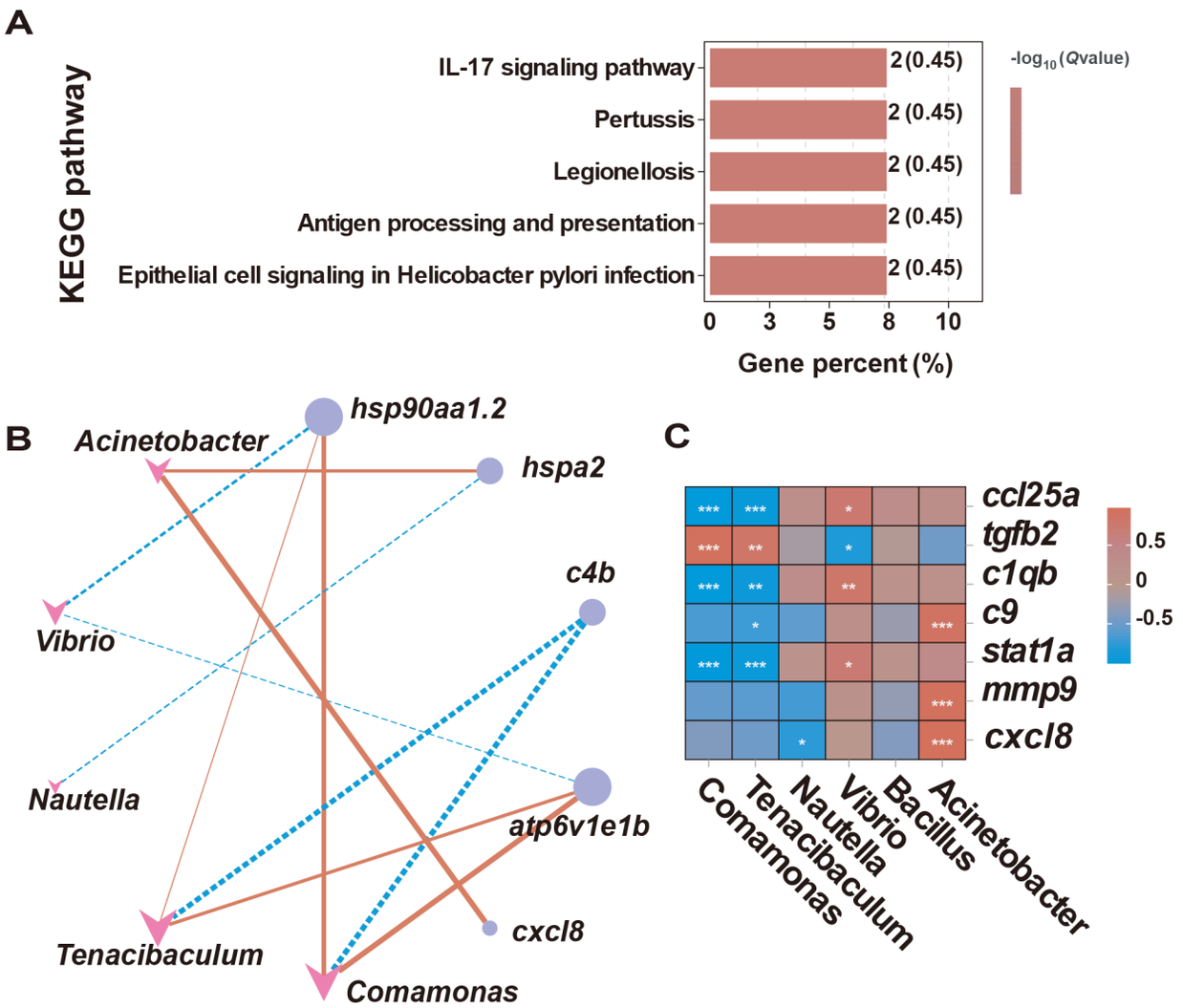

Figure 6 Integrated analysis of larval transcriptome and microbiome

A: KEGG pathway enrichment analysis of genes associated with the transcriptome and microbiome. B: Gene-microbe association networks. Nodes: Genes (circles), microbes (arrows); Node size: Relative abundance; Edges: Spearman correlations (red solid=positive; blue dashed: Negative); Edge width: Correlation strength. C: Spearman correlations between expression of immune-related genes and relative abundance of dominant larval microbial taxa. *: P<0.05; **: P<0.01; ***: P<0.001.

recapitulated in zebrafish under immune constraints, suggesting immune-regulated microbial remodeling (Figure 7D–F). Notably, *in vitro* assays confirmed that DXMS had no direct inhibitory effect on four intestinal *Vibrio* strain (Supplementary Figure S2, P>0.05), suggesting host-mediated ecological shifts rather than compound toxicity (Supplementary Table S4).

Intestinal barrier compromised under immune constraints

Histological analyses revealed that DXMS induced dose-dependent mucosal alterations (Figure 8A, B). PAS staining showed a significant increase in goblet cell density per villus length across treatment groups T1–T3 (P<0.05, Figure 8C). H&E staining demonstrated progressive reductions in villus height and width, particularly in the high concentration group (T3) (P<0.05, Figure 8D, E), although lamina propria width remained unchanged (P>0.05, Figure 8F). Epithelial thickness declined to its lowest level in T2 and partially recovered in T3 (P<0.05), accompanied by microvillar shortening and epithelial cell edema (Figure 8E). High-dose DXMS (T3) also induced lamina propria vacuolation and edema (Figure 8G). Immune constraints disrupted both the mucous and mechanical barriers. The expression of *muc2.1* significantly increased in T2 but declined sharply in T3 (P<0.05), while *muc5.1* remained stable (P>0.05, Figure 8H). Tight junction genes (*tjp1a* and *cldn15la*) and adherens junction gene (*ctnnb1*) were significantly up-regulated in T2 (P<0.05) but returned to baseline levels in T3 (Figure 8I). The expression of *cldnb* progressively declined with increasing DXMS concentrations (P<0.05). Notably, the expression pattern of *cldn15la* in zebrafish intestine closely paralleled that of *L. crocea* (Figure 8J).

DISCUSSION

The processes governing the initial colonization and succession of symbiotic microbial communities in fish remain incompletely resolved, particularly regarding the extent and mechanisms of host-mediated regulation (Auclert et al., 2024). This study systematically characterized microbiota compositional dynamics and community assembly in early-stage *L. crocea*, revealing that larval microbial transitions are jointly driven by stochastic environmental acquisition and host-driven deterministic selection. Notably, DPH3–DPH18

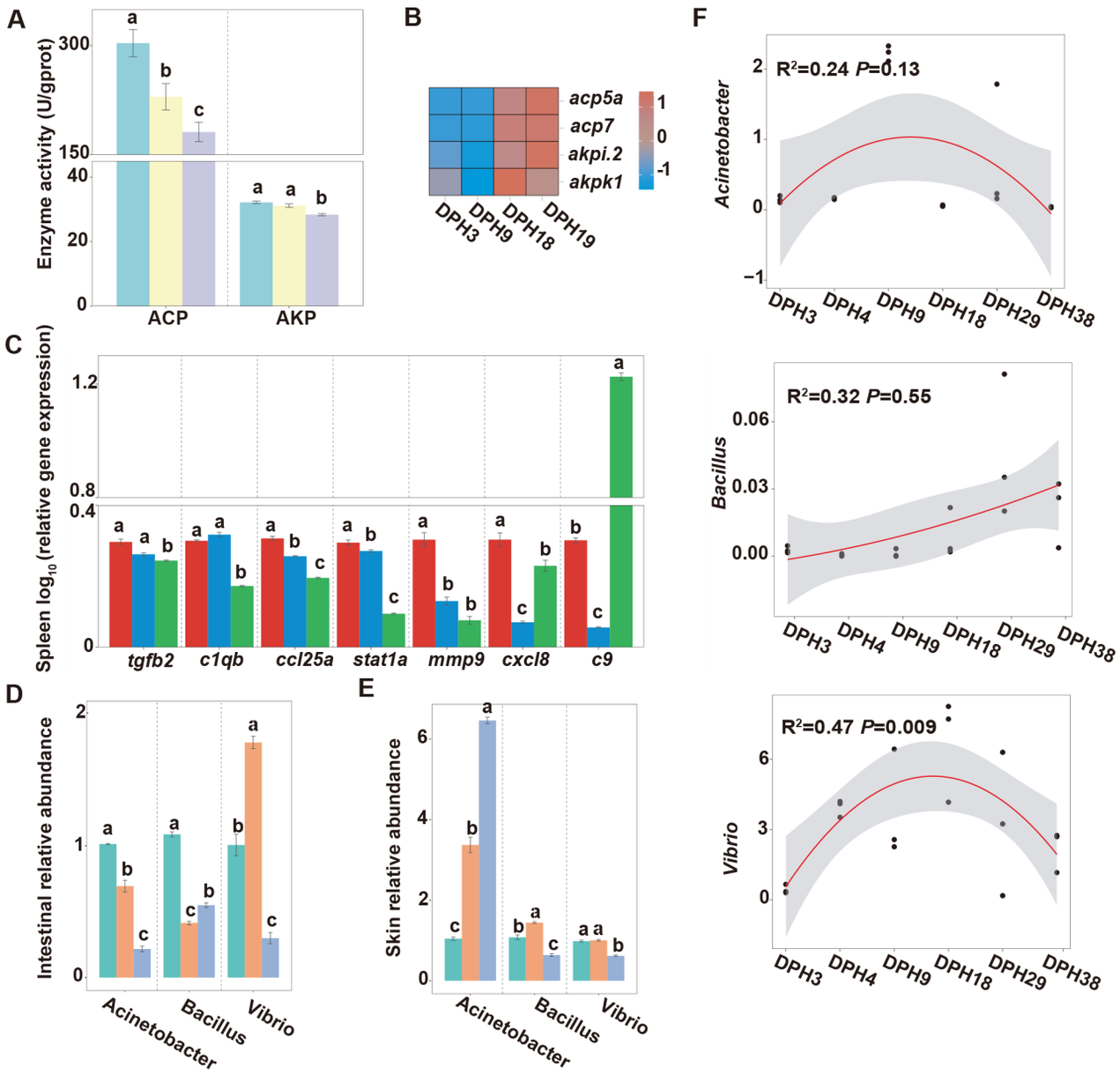

Figure 7 Assessment of immune constraints in zebrafish and dynamics of core microbial taxa

A: Nonspecific immune indices in zebrafish. ACP: Acid phosphatase, AKP: Alkaline phosphatase. Data are presented as mean±SD. B: Heatmap of ACP- and AKP-associated microbial genes from *Larimichthys crocea* microbiota. C: Relative expression of immune-related genes in zebrafish spleen under varying DXMS concentrations. D: Relative abundance of *Acinetobacter* and *Vibrio* in zebrafish intestine. E: Relative abundance of *Acinetobacter*, *Bacillus*, and *Vibrio* in zebrafish skin. F: Temporal changes in abundance of *Acinetobacter*, *Bacillus*, and *Vibrio* in *L. crocea* microbiota. Different lowercase superscripts denote significant differences (P<0.05).

represented a critical window during which host immunity significantly influenced microbial colonization trajectories. Functional cross-species validation in zebrafish substantiated this conclusion, confirming conserved host-microbiota interactions and highlighting the threshold-dependent immune effects on epithelial barrier integrity.

Microbial α-diversity exhibited a marked temporal association with larval age, reaching maximal richness and evenness at DPH18. This pattern was consistent with findings in other teleost species such as *Cyprinus carpio* and *Seriola dumerili* (Supplementary Table S5), although peak diversity occurred at distinct developmental stages (Zhang et al., 2024; Zhao et al., 2024). However, cross-species comparisons across eight fish species (Supplementary Table S3) failed to reveal consistent associations between α-diversity trends and ecological variables, such as feeding strategy or habitat preference, indicating that microbiota dynamics are predominantly shaped by host-intrinsic developmental programs rather than environmental filtering (Sumithra et al., 2024). Notably, the α-diversity peak at DPH18 coincided with maximal abundance of *Vibrio*, a genus comprising opportunistic pathogens known for causing infections in immunocompromised hosts (Manchanayake et al., 2023). Similar patterns have been observed in marine larvae, where transient increases in *Vibrio* are linked to vulnerability in innate immune defenses (Muñoz-Cerro et al., 2024; Schwaner et al., 2024). The subsequent reduction in microbial diversity after DPH18 paralleled a transition toward increasingly selective microbial niches, with *Comamonas*-dominated communities emerging. This compositional shift mirrors observations in

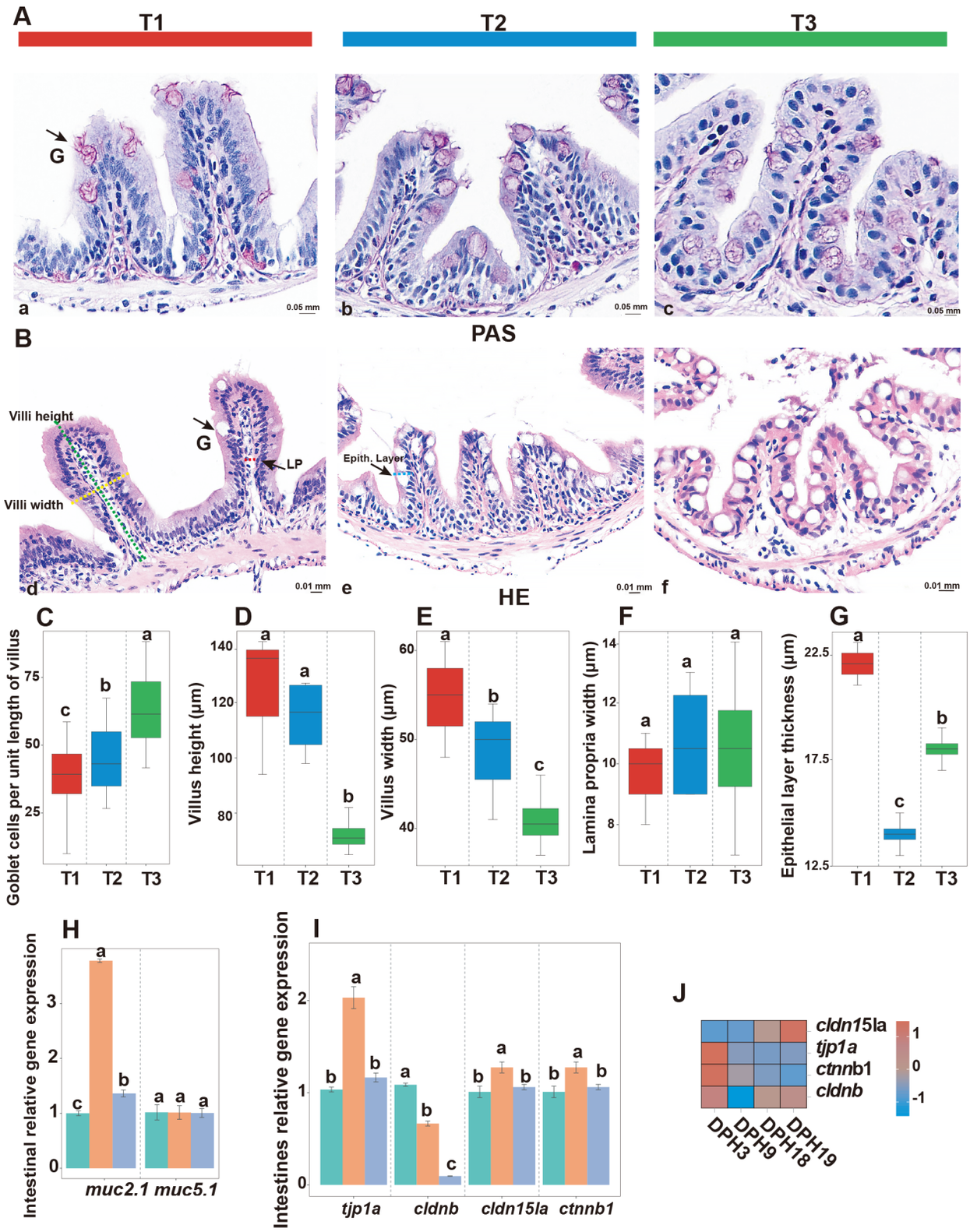

Figure 8 Intestinal histopathology and barrier disruption in zebrafish following DXMS exposure

A: PAS staining of intestinal sections from T1, T2, and T3 groups. Scale bar: 0.05 mm. B: H&E staining of corresponding sections. Scale bar: 0.01 mm. G: Goblet cell; Lp: Lamina propria. Dashed lines: Villus height (green), villus width (yellow), lamina propria width (red), and epithelial thickness (blue). C–G: Quantification of goblet cell density (C), villus height (D), villus width (E), lamina propria width (F), and epithelial thickness (G) across groups after 7 days of DXMS treatment. H: Relative expression of mucosal barrier-related genes. I: Relative expression of tight and adherens junction-related genes. J: Heatmap of tight and adherens junction-related genes from *Larimichthys crocea* microbiome. Different lowercase superscripts denote significant differences (P<0.05).

Pacific white shrimp (*Penaeus vannamei*), where *Vibrio* spp. dominate during juvenile stages under pathogen-driven selective pressure (Ramirez et al., 2022).

Larval microbiota in *L. crocea* primarily originated through

self-propagation, accounting for over 20% of total inputs, while contributions from dietary and water sources remained negligible. These findings support early host-mediated filtering as a dominant force in microbial assembly, consistent with patterns observed in Chinese mitten crab (*Eriocheir sinensis*) and oyster (*Crassostrea sikamea*) larvae (Dai et al., 2022; Lu et al., 2022). However, maternal transmission likely contributed additional microbial seeding, as documented in *Portunus trituberculatus* (Sun et al., 2025) and terrestrial animals (Bi et al., 2019; Li et al., 2022; Yang et al., 2025), suggesting that external source estimates may underrepresent inherited microbial inputs. Despite limited long-term colonization, environmental and dietary microbes may serve as transient reservoirs for early-stage microbial seeding. Functional convergence analysis via BugBase at DPH3 identified shared phenotypic profiles between larval and water-derived microbiota despite minimal taxonomic overlap, suggesting that host selection filters microbes based on functional traits rather than taxonomic identity. Similar trait-based filtering has been reported in coral larvae exposed to oligotrophic environments (Marangon et al., 2023; Sha et al., 2025). The diminishing correlation between larval and diet-associated communities beyond DPH18 further suggests a developmental shift from passive environmental acquisition to selective host-driven microbial recruitment.

NCM also identified DPH18 as a pivotal transitional point characterized by a transient peak in stochastic processes. Between DPH3 and DPH18, microbial assembly was predominantly shaped by stochastic dispersal and ecological drift, as evidenced by maximal NCM fit (R^2=0.71) and migration rate (m=0.88) at DPH18, reflecting minimal selective pressure. However, the marked decline in NCM fit at DPH38 (R^2=0.6) signaled a shift toward increasing deterministic influence. This hump-shaped neutrality trajectory mirrors patterns reported in turbot (*Scophthalmus maximus*) larvae (Gomes et al., 2025). Null model partitioning further confirmed the concurrent operation of stochastic and deterministic forces across developmental stages. Notably, βNTI values clustered near stochastic thresholds throughout, indicating persistent deterministic inputs even during neutrality-dominated phases. At DPH18, homogeneous selection accounted for 51.2% of community structuring, while dispersal limitation contributed 37.3%, preserving niche heterogeneity, functional specialization, and ecological resilience. The subsequent βNTI increase at DPH38 likely reflects intensified deterministic selection acting on stable symbionts, coupled with stochastic turnover in transient microbiota compartments (Du et al., 2025). Microbiota assembly in *L. crocea* thus followed a dual-phase strategy—initial stochastic seeding followed by deterministic filtering—with DPH18 marking a critical inflection point. This biphasic pattern aligns with observations in zebrafish, where host immune maturation restricts environmental microbial persistence after defined developmental windows (Burns et al., 2016).

Early ontogeny demands simultaneous containment of pathogenic threats and accommodation of beneficial symbionts during immune maturation (Ignacio et al., 2024). Our findings indicated that *L. crocea* larvae may navigate early developmental challenges through tightly orchestrated immune modulation. Transcriptomic profiling revealed a pronounced functional disequilibrium in early immune activity. Innate immune pathways such as complement and coagulation cascades and IL-17 signaling were strongly up-regulated, yet pro-inflammatory mediators, including *cxcl8*, *mmp9*, *c9*, *c7b*, *c3*, and *cebpb*, reached maximal expression at DPH18, coinciding with peak microbial α-diversity. At the same stage, the anti-inflammatory regulator *tgfb2* was markedly suppressed. Reduced *tgfb2* expression is known to attenuate immune-mediated microbial clearance and facilitate opportunistic colonization (Sager et al., 2021; Sitarik et al., 2017; Torres-Castro et al., 2018). This immune permissive state aligned with the highest NCM fit and peak migration rate (m), coinciding with peak microbial α-diversity at DPH18. The delayed rise of deterministic selection corresponded with the resurgence of *Comamonas* dominance, suggesting that immune-driven permissiveness is transient and developmentally encoded. The synergistic interplay between weaning-associated microbial dynamics and host immune maturation has also been reported in mammals (Lubin et al., 2023; Trigo et al., 2024). These findings suggest that *L. crocea* larvae may exploit brief periods of reduced immune constraints as developmental “windows of opportunity”, during which early microbial communities gain a foothold before selective forces consolidate a stable and host-adapted microbiota.

DXMS-induced constraints mirrored immune developmentally programmed microbial modulation in *L. crocea*. Increasing DXMS concentration markedly reduced the expression of spleen-derived immune genes such as *c1qb*, *stat1a*, and *ccl25a*, accompanied by substantial fluctuations in the abundance of *Acinetobacter, Bacillus*, and *Vibrio*. These shifts demonstrated that immune suppression destabilizes microbial homeostasis (Falcão et al., 2022; Lee-Estevez et al., 2018). In *L. crocea* larvae, the relative abundance of these taxa rose progressively from DPH3 to DPH18, mirroring the expression trajectories of *c9*, *c7b*, *cxcl8*, *mmp9*, *cebpb*, *stat1a*, *c1qb*, and *ccl25a*, and showing inverse correspondence with *tgfb2*. Comparable patterns have been reported in mice, where parasites exploit immature host immunity to facilitate colonization (Dessein et al., 2020; Wang et al., 2021). The degree of immune constraint during early colonization appeared pivotal for barrier function in fish larvae. Notably, moderate suppression (T2) triggered compensatory enhancement of mucosal defenses, reflected in increased goblet cell density (Yang & Yu, 2021), together with transient elevation of mucus- (*muc2.1*) and tight junction-associated (*tjp1a*, *cldn15la*) genes. These responses indicate that localized barrier fortification (e.g., thickened mucus layers and reinforced intercellular junctions) balances the risks introduced by reduced immune activity (He et al., 2023; Wang et al., 2021). In contrast, high-dose immune restriction (T3) induced villus atrophy, epithelial edema, and persistent down-regulation of *cldnb*, highlighting a threshold beyond which barrier function deteriorates, thereby enabling taxa such as intestinal *Acinetobacter* to expand. Notably, the synchronized expression pattern of *cldn15la* and intestinal *Acinetobacter* and *Bacillus* abundance recovery in *L. crocea* and zebrafish may reflect conserved developmental species-crosstalk Dynamic regulation of tight and adherens junction may prolong stochastic colonization phases, allowing early microbial assemblages to establish before deterministic selection consolidates stable symbiotic communities (Sitarik et al., 2017).

CONCLUSION

In summary, our findings demonstrated that during early

developmental stages, *L. crocea* larvae underwent rapid microbial community assembly and succession, driven synergistically by host-mediated selection and environment. Notably, DPH18 emerged as a pivotal developmental inflection point, characterized by maximal α-diversity and peak alignment with NCM predictions. Transcriptomic profiling further revealed that up-regulation of *c1qb*, *ccl25a*, and *mmp9* enhanced chemotaxis and extracellular matrix remodeling, while concurrent suppression of *tgfb2* attenuated phagocytic clearance, facilitating microbial niche establishment. These findings support the existence of a transient "window of opportunity" during which immune constraints permit colonization by diverse microbial taxa without compromising host defense. Dose-dependent experiments in zebrafish further demonstrated that moderate immune constraints (T2) permitted transient pathogen proliferation alongside epithelial fortification. Collectively, these results identified DPH3–DPH18 as a conserved developmental window during which larval hosts transiently tolerate opportunistic colonization to enable microbiota assembly, ultimately supporting long-term host-microbe homeostasis.

DATA AVAILABILITY

The raw 16S rRNA sequence data generated in this study were deposited in the Sequence Read Archive (BioProjectID PRJNA1229166). Transcriptomic data were deposited in the Sequence Read Archive (BioProjectID PRJNA1229192), National Genomics Data Center (CRA047619), and Science Data Bank (https://doi.org/10.57760/sciencedb.j00139.00256). All data that support the findings of this study are available from the corresponding author upon reasonable request.

SUPPLEMENTARY DATA

Supplementary data to this article can be found online.

COMPETING INTERESTS

The authors declare that they have no competing interests.

AUTHORS' CONTRIBUTIONS

R.J.L.: Methodology, Visualization, Writing - original draft, Data Curation. Z.J.Z.: Resources, Investigation. Z.Q.Q.: Investigation, Validation. X.Y.: Formal analysis, Validation. Q.W.M.: Methodology, Investigation. B.Y.: Methodology, Resources. J.Y.Z: Methodology, Investigation. X.B.B.: Investigation. N.Z.: Conceptualization, Investigation, Writing-Review & Editing, Supervision, Funding acquisition. B.Z.: Conceptualization, Writing-Review & Editing, Supervision, Project administration. All authors read and approved the final version of the manuscript.

ACKNOWLEDGMENTS

We gratefully acknowledge all members of the Southern Marine Science and Engineering Guangdong Laboratory-Zhanjiang who contributed to this study.

REFERENCES

Arevalo E, Cabral HN, Villeneuve B, et al. 2023. Fish larvae dynamics in temperate estuaries: a review on processes, patterns and factors that determine recruitment. *Fish and Fisheries*, **24**(3): 466–487.

Auclert LZ, Chhanda MS, Derome N. 2024. Interwoven processes in fish development: microbial community succession and immune maturation. *PeerJ*, **12**: e17051.

Ba XB, Zhuang ZJ, Zhou ZB, et al. 2025. Taurine related pathways effect the potential domestication of wild *Larimichthys crocea* adapt to stress environment. *Aquaculture*, **605**: 742532.

Bandara KA, Politis SN, Sganga DE, et al. 2024. Effects of European eel egg and larval stocking density on rearing water, offspring bacteriome and derived immune response. *Aquaculture*, **585**: 740716.

Bi YL, Cox MS, Zhang F, et al. 2019. Feeding modes shape the acquisition and structure of the initial gut microbiota in newborn lambs. *Environmental Microbiology*, **21**(7): 2333–2346.

Burns AR, Stephens WZ, Stagaman K, et al. 2016. Contribution of neutral processes to the assembly of gut microbial communities in the zebrafish over host development. *The ISME Journal*, **10**(3): 655–664.

Chen WD, Ren KX, Isabwe A, et al. 2019. Stochastic processes shape microeukaryotic community assembly in a subtropical river across wet and dry seasons. *Microbiome*, **7**(1): 138.

Dai WF, Ye J, Liu S, et al. 2022. Bacterial community dynamics in Kumamoto oyster *Crassostrea sikamea* hatchery during larval development. *Frontiers in Microbiology*, **13**: 933941.

Darrigues J, van Meerwijk JPM, Romagnoli P. 2018. Age-dependent changes in regulatory T lymphocyte development and function: a mini-review. *Gerontology*, **64**(1): 28–35.

Deng YL, Kokou F, Verdegem MCJ, et al. 2025. Impact of early life rearing conditions on feed intake, growth, nutrient digestion and energy metabolism of Nile tilapia in later life. *Aquaculture*, **598**: 742042.

Dessein R, Bauduin M, Grandjean T, et al. 2020. Antibiotic-related gut dysbiosis induces lung immunodepression and worsens lung infection in mice. *Critical Care*, **24**(1): 611.

Du Y, Zhang L, Yang Y, et al. 2025. Assembly, network and functional compensation of specialists and generalists in poplar rhizosphere under salt stress. *npj Biofilms and Microbiomes*, **11**(1): 28.

Falcão MAP, dos Santos Dantas MC, Rios CT, et al. 2022. Zebrafish as a tool for studying inflammation: a systematic review. *Reviews in Fisheries Science & Aquaculture*, **30**(1): 101–122.

Fernandes VMC, Rudgers JA, Collins SL, et al. 2022. Rainfall pulse regime drives biomass and community composition in biological soil crusts. *Ecology*, **103**(9): e3744.

Gensollen T, Iyer SS, Kasper DL, et al. 2016. How colonization by microbiota in early life shapes the immune system. *Science*, **352**(6285): 539–544.

Gomes NCM, Cleary DFR, Silva DAM, et al. 2025. Shifts in turbot (*Scophthalmus maximus*) larvae bacterial communities from neutrality to non-neutrality: a window of opportunity for microbiome interventions. *Aquaculture*, **599**: 742074.

He WH, Wang JH, Han MY, et al. 2023. Potential toxicity and mechanisms of T-2 and HT-2 individually or in combination on the intestinal barrier function of porcine small intestinal epithelial cells. *Toxins*, **15**(12): 682.

Hou DW, Li HY, Wang S, et al. 2024a. Nitrite nitrogen stress disrupts the intestine bacterial community by altering host-community interactions in shrimp. *Science of the Total Environment*, **925**: 171536.

Hou DW, Zhou RJ, Deng ZX, et al. 2024b. Environmental dispersal and host priority effect alternatively dominate intestinal microbiota succession of cultured shrimp along with host development. *Marine Life Science & Technology*, **6**(4): 690–699.

Ignacio A, Czyz S, Mccoy KD. 2024. Early life microbiome influences on development of the mucosal innate immune system. *Seminars in Immunology*, **73**: 101885.

Kim KI, Won KM, Lee ES, et al. 2019. Detection of *Vibrio* and ten *Vibrio* species in cage-cultured fish by multiplex polymerase chain reaction using house-keeping genes. *Aquaculture*, **506**: 417–423.

Knights D, Kuczynski J, Charlson ES, et al. 2011. Bayesian community-wide culture-independent microbial source tracking. *Nature Methods*, **8**(9): 761–763.

Kumar S, Stecher G, Li M, et al. 2018. MEGA X: molecular evolutionary genetics analysis across computing platforms. *Molecular Biology and*

Evolution, **35**(6): 1547–1549.

Lee-Estevez M, Figueroa E, Cosson J, et al. 2018. Zebrafish as a useful model for immunological research with potential applications in aquaculture. *Reviews in Aquaculture*, **10**(1): 213–223.

Li XB, Bi R, Xiao KP, et al. 2022. Hen raising helps chicks establish gut microbiota in their early life and improve microbiota stability after H9N2 challenge. *Microbiome*, **10**(1): 14.

Liu BW, Guo HY, Liu BS, et al. 2024. Early development and allometric growth patterns of *Larimichthys crocea* (Richardson, 1846). *Aquaculture*, **584**: 740642.

Livak KJ, Schmittgen TD. 2001. Analysis of relative gene expression data using real-time quantitative PCR and the 2^{-ddCT} method. *Methods*, **25**(4): 402–408.

Lu ZB, Ren ZM, Lin WC, et al. 2022. Succession, sources, and assembly of bacterial community in the developing crab larval microbiome. *Aquaculture*, **548**: 737600.

Lubin JB, Green J, Maddux S, et al. 2023. Arresting microbiome development limits immune system maturation and resistance to infection in mice. *Cell Host & Microbe*, **31**(4): 554–570. e7.

Manchanayake T, Salleh A, Amal MNA, et al. 2023. Pathology and pathogenesis of *Vibrio* infection in fish: a review. *Aquaculture Reports*, **28**: 101459.

Marangon E, Uthicke S, Patel F, et al. 2023. Life-stage specificity and cross-generational climate effects on the microbiome of a tropical sea urchin (Echinodermata: Echinoidea). *Molecular Ecology*, **32**(20): 5645–5660.

Muñoz-Cerro K, González R, Mercado A, et al. 2024. Scallop larvae resistant to a pathogenic *Vibrio* harbor host-associated bacteria with probiotic potential. *Aquaculture*, **579**: 740217.

Nie L, Wu XY, Zhao ZY, et al. 2025. Palmitoylation-mediated NLRP3 inflammasome activation in teleosts highlights evolutionary divergence in immune regulation. *Zoological Research*, **46**(1): 3–14.

Nikouli E, Meziti A, Antonopoulou E, et al. 2019. Host-associated bacterial succession during the early embryonic stages and first feeding in farmed Gilthead Sea Bream (*Sparus aurata*). *Genes*, **10**(7): 483.

Nunez H, Nieto PA, Mars RA, et al. 2025. Early life gut microbiome and its impact on childhood health and chronic conditions. *Gut Microbes*, **17**(1): 2463567.

Pan YR, Han XQ, Tian TT, et al. 2025. Single-cell atlas of grass carp (*Ctenopharyngodon idella*) peripheral blood IgM^+ B cells provides insights into B cell-mediated immune responses in teleost fish. *Zoological Research*, **46**(5): 953–966.

Paralika V, Kokou F, Karapanagiotis S, et al. 2023. Characterization of host-associated microbiota and isolation of antagonistic bacteria from Greater Amberjack (*Seriola dumerili*, Risso, 1810) larvae. *Microorganisms*, **11**(8): 1889.

Peng SJ, Ye LJ, Li YX, et al. 2024. Metagenomic insights into jellyfish-associated microbiome dynamics during strobilation. *ISME Communications*, **4**(1): ycae036.

Ramirez M, Domínguez-Borbor C, Salazar L, et al. 2022. The probiotics *Vibrio diabolicus* (Ili), *Vibrio hepatarius* (P62), and *Bacillus cereus sensu stricto* (P64) colonize internal and external surfaces of *Penaeus vannamei* shrimp larvae and protect it against *Vibrio parahaemolyticus*. *Aquaculture*, **549**: 737826.

Rimoldi S, Quiroz KF, Kalemi V, et al. 2025. Interactions between nutritional programming, genotype, and gut microbiota in Atlantic salmon: long-term effects on gut microbiota, fish growth and feed efficiency. *Aquaculture*, **596**: 741813.

Rosado D, Pérez-Losada M, Severino R, et al. 2022. Monitoring infection and antibiotic treatment in the skin microbiota of farmed European Seabass (*Dicentrarchus labrax*) fingerlings. *Microbial Ecology*, **83**(3): 789–797.

Sager REH, Walker AK, Middleton F, et al. 2021. Trajectory of change in brain complement factors from neonatal to young adult humans. *Journal of Neurochemistry*, **157**(3): 479–493.

Schuh NW, Carrier TJ, Schrankel CS, et al. 2020. Bacterial exposure mediates developmental plasticity and resistance to lethal *Vibrio lentus* infection in purple sea urchin (*Strongylocentrotus purpuratus*) larvae. *Frontiers in Immunology*, **10**: 3014.

Schwaner C, Barbosa M, Haley J, et al. 2024. Transcriptomics, proteomics, and physiological assays reveal immunosuppression in the eastern oyster *Crassostrea virginica* exposed to acidification stress. *Fish & Shellfish Immunology*, **146**: 109366.

Sha HN, Lu YM, Zhan PP, et al. 2025. Beneficial effects of probiotics on *Litopenaeus vannamei* growth and immune function via the recruitment of gut *Rhodobacteraceae* symbionts. *Zoological Research*, **46**(2): 388–400.

Sitarik AR, Bobbitt KR, Havstad SL, et al. 2017. Breast milk transforming growth factor β is associated with neonatal gut microbial composition. *Journal of Pediatric Gastroenterology and Nutrition*, **65**(3): e60–e67.

Sumithra TG, Sharma SRK, Suresh G, et al. 2024. Mechanistic insights into the early life stage microbiota of silver pompano (*Trachinotus blochii*). *Frontiers in Microbiology*, **15**: 1356828.

Sun Y, Lin WC, Wu QY, et al. 2025. Bacterial dynamics and biotic sources in the developing swimming crab embryos. *Aquaculture*, **595**: 741523.

Torres-Castro P, Abril-Gil M, Rodríguez-Lagunas MJ, et al. 2018. TGF-β2, EGF, and FGF21 growth factors present in breast milk promote mesenteric lymph node lymphocytes maturation in suckling rats. *Nutrients*, **10**(9): 1171.

Trigo NF, Kalbermatter C, Yilmaz B, et al. 2024. The protective effect of the intestinal microbiota in type-1 diabetes in NOD mice is limited to a time window in early life. *Frontiers in Endocrinology*, **15**: 1425235.

Wang R, Moniruzzaman M, Wong KY, et al. 2021. Gut microbiota shape the inflammatory response in mice with an epithelial defect. *Gut Microbes*, **13**(1): 1887720.

Wei YW, Zhang SY, Guan GK, et al. 2023. A specific and rapid method for detecting *Bacillus* and *Acinetobacter* species in Daqu. *Frontiers in Bioengineering and Biotechnology*, **11**: 1261563.

Woelfel S, Silva MS, Stecher B. 2024. Intestinal colonization resistance in the context of environmental, host, and microbial determinants. *Cell Host & Microbe*, **32**(6): 820–836.

Yang J, Xu ZK, Wang XY, et al. 2025. Parents greater influenced the fecal microbiome and resistome of ibis nestlings than artifical breeding environment contamination. *Environmental Research*, **271**: 121057.

Yang SW, Yu M. 2021. Role of goblet cells in intestinal barrier and mucosal immunity. *Journal of Inflammation Research*, **14**: 3171–3183.

Yin ZY, Liu QD, Liu YT, et al. 2021. Early life intervention using probiotic *Clostridium butyricum* improves intestinal development, immune response, and gut microbiota in large yellow croaker (*Larimichthys crocea*) larvae. *Frontiers in Immunology*, **12**: 640767.

Zhang JH, Liu Y, Shan SJ, et al. 2024. Variation in the gut microbiota during the early developmental stages of common carp (*Cyprinus carpio* L.) and its correlation with feed and pond water microflora. *BMC Veterinary Research*, **20**(1): 464.

Zhao N, Guo JM, Zhang B, et al. 2022. Heterogeneity of the tissue-specific mucosal microbiome of normal grass carp (*Ctenopharyngodon idella*). *Marine Biotechnology*, **24**(2): 366–379.

Zhao N, Li RJ, Zhu XF, et al. 2024. Host development promotes the early microbiota succession of teleost surpassing dietary management. *Aquaculture*, **593**: 741309.